Numerical solutions and laser-Doppler measurements of spin-up

By ALEX WARN-VARNAS

Naval Research Laboratory, Washington D.C. 20375†

WILLIAM W. FOWLIS,

Florida State University, Tallahassee‡

STEVE PIACSEK,

Naval Research Laboratory, Washington D.C. 20375†

AND SANG MYUNG LEE

Florida State University, Tallahassee

The spin-up flow in a cylinder of homogeneous fluid has been examined both experimentally and numerically. The primary motivation for this work was to check numerical solution schemes by comparing the numerical results with laboratory measurements obtained with a rotating laser-Doppler velocimeter. The laser-Doppler technique is capable of high accuracy with small space and time resolution, and disturbances of the flow are virtually negligible. A series of measurements was made of the zonal flow over a range of Ekman numbers ($1 \cdot 06 \times 10^{-3} \leqslant E \leqslant 3 \cdot 30 \times 10^{-3}$) and Rossby numbers ($0 \cdot 10 \leqslant |\epsilon| \leqslant 0 \cdot 33$) at various locations in the interior of the flow. These measurements exceed previous ones in accuracy. The weak inertial modes excited by the impulsive start are detectable. The numerical simulations used the primitive equations in axisymmetric form and employed finite-difference techniques on both constant and variable grids. The number of grid points necessary to resolve the Ekman layers was determined. A thorough comparison of the simulations and the experimental measurements is made which includes the details of the amplitude and frequency of the inertial modes. Agreement to within the experimental tolerance is achieved. Analytical results for conditions identical to those in the experiments are not available but some similar linear and nonlinear theories are also compared with the experiments.

1. Introduction

The new laser-Doppler technique for fluid flow measurement introduced by Yeh & Cummins (1964) has enabled experimentalists to obtain accurate velocity measurements with virtually no disturbance of the flow. This technique is particularly helpful for measurements in contained and rotating laboratory flows, where conventional probes often significantly disturb the flow (Fultz & Kaiser 1971; Cerasoli 1975). It has been recognized recently that such measurements can provide a powerful method for

† Present address: Naval Ocean Research and Development Activity, Bay St Louis, Mississippi. 39520.

‡ Present address: NASA, Marshall Space Flight Center, Alabama 35812.

the evaluation of the accuracy of numerical simulation techniques. The primary motivation for this research was to check numerical simulation schemes by comparing them with accurate and disturbance-free laser-Doppler measurements of spin-up.

This paper describes an experimental and numerical investigation of the flow resulting from the spin-up of a homogeneous fluid in a cylindrical container. This spin-up (spin-down) experiment consisted of suddenly increasing (decreasing) the rotation rate of a cylindrical fluid container and examining the transient fluid motions which adjust the fluid from one state of solid-body rotation to the other. Weak inertial oscillations are excited by the change in rotation rate. For an excellent review of work on spin-up see Benton & Clark (1974). Greenspan & Howard (1963) showed that, for a relatively strong rotation rate and for a small change in the rotation rate, three time scales are involved in the complete spin-up process. First Ekman layers form on the horizontal surfaces on a time scale $2/\Omega$, where Ω is the rotation rate. In these Ekman layers fluid moves radially outwards and is replaced by fluid drawn from the interior. In the interior, fluid moves radially inwards to replace the fluid removed and conserves angular momentum as it moves. This process spins up the interior on a time scale given by $h/(\nu\Omega)^{\frac{1}{2}}$, where h is the half-depth of the fluid and ν is the kinematic viscosity. Finally, all motions decay on a diffusion time scale of h^2/ν.

The experimental results presented by Fowlis & Martin (1975) and the results presented in this paper were obtained in a cylinder with a rigid top which was in contact with the water which filled the container. The laser-Doppler technique was used to measure the zonal flow for several rotation rates, for several changes in rotation rate $\Delta\Omega$ and for different radial and depth locations (r, z) within the cylinder. The accuracy, spatial resolution and time resolution of the technique are such that the weak intertial modes could be identified clearly. The relevant dimensionless parameters are the Ekman number $E \equiv \nu/\Omega_i h^2$, where Ω_i is the initial rotation rate, and the Rossby number $\epsilon \equiv \Delta\Omega/\Omega_i$. The choice of Ω_i rather than the final rotation rate Ω_f for scaling purposes is based upon the fact that the nonlinear spin-up theories show that even for moderate ϵ the spin-up time is given more accurately by a time defined using Ω_i. The experiments were carried out for parameter ranges

$$1{\cdot}06 \times 10^{-3} \leqslant E \leqslant 3{\cdot}30 \times 10^{-3}, \quad 0{\cdot}100 \leqslant |\epsilon| \leqslant 0{\cdot}333.$$

There is no experimental or theoretical evidence to suggest that for these parameter ranges the flow should not be axisymmetric.

Numerical simulations were carried out for conditions almost identical to the experimental conditions. The simulations used the primitive equations in axisymmetric form and employed finite-difference techniques on a staggered mesh. Both constant and variable grids with corresponding different spatial and time differencing schemes were tried and the results compared with one another and with the experimental results. The particular question of how many grid points should be used in the top and bottom Ekman layers, the thinnest boundary layers in the system, was investigated. The numerical and experimental results for the zonal velocity at different locations within the cylinder are superimposed to exhibit the excellent agreement which was obtained.

Detailed analytical results for the same conditions as in the experiments described in this paper are not available. Greenspan & Howard (1963) carried out a linearized analysis for spin-up between two infinite parallel disks which included the inertial
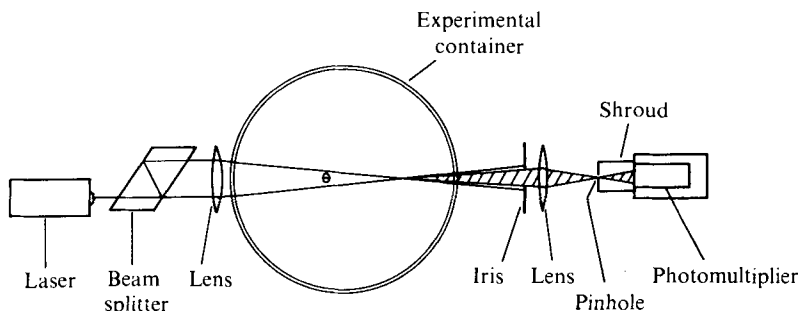
FIGURE 1. A schematic drawing showing the essential geometry
of the dual-scatter LDV system.

oscillations and a comparison is made of their results with the experimental results. Later workers extended this analysis to include nonlinear effects and finite geometry and some of these results are discussed and also compared with the experimental results.

2. Experimental apparatus and procedures

This section includes a description of the experimental apparatus and procedure and a very brief description of the laser-Doppler technique; further details and references on this technique are given in Fowlis & Martin (1975), Adrian & Goldstein (1971) and George & Lumley (1973). The parameters for the spin-up experiments are given in §4 and tables 1 and 2 and the results are shown in figures 8–16.

A right circular Plexiglas cylinder (inner diameter $2b = 18.98 \pm 0.01$ cm, depth $2h = 6.04 \pm 0.01$ cm) with a rigid lid was filled with water and mounted with its axis of symmetry vertical on a horizontal turntable. The turntable (Genisco Model 1147-2) had an oil hydrostatic bearing and a direct drive controlled by a d.c. feedback loop. The error in Ω was almost always less than 1 in 5000 and the error in $\Delta\Omega$ always less than 1 in 500. In order for the imposed change in angular velocity to be considered impulsive, $\Delta\Omega$ should be accomplished in a time small compared with the shortest time scale of the problem $(2/\Omega_i)$. The changes were performed as quickly as the turntable system would allow. The angular acceleration $\dot{\Omega}$ was constant; for increases in Ω, $\dot{\Omega} = 0.12$ s^{-2}, and for decreases, $\dot{\Omega} = 0.15$ s^{-2}. The above requirement for an impulsive change can be written as $\Omega_i \Delta\Omega/2\dot{\Omega} \ll 1$. For the worst case (table 1, figure 11*b*) this ratio was equal to 0.82 but for most of the experiments the ratio was less than 0.37, thus most of the experiments can be considered as approximately impulsive.

The relative zonal flow velocity was measured using a laser-Doppler velocimeter (LDV) mounted on and attached to the turntable. Figure 1 is a plan view showing the essential geometry of the dual-scatter LDV system chosen. A helium–neon laser (Spectra-Physics, Model 120) was used. The location of the flow measurement is at the cross-over point of the laser beams. The flow speed was determined from a measurement of the Doppler frequency shift of the scattered light. The relationship between the flow velocity v and the Doppler frequency ν_D is $v = \lambda\nu_D/2n\sin\frac{1}{2}\theta$, where λ is the wavelength of the laser light (in vacuo), n is the refractive index of the fluid and θ is the angle between the beams. For the experiments described in this paper θ varied

between 7·30° and 8·11°, the measured values of ν_D ranged from about 110 to 2700 s^{-1} and the corresponding values of v from about 0·036 to 0·91 cm s^{-1}. Small polystyrene spheres (diameter 0·5 μm) were added to the water in a concentration ratio of about 3×10^{-6} by volume to enhance the scattered signal. There is no theoretical or experimental evidence to suggest that effects due to the scatterers or the weak absorption of the laser light produced noticeable disturbances of the flow.

The output signal from the photomultiplier (Centronic, type P4283B) was taken off the turntable by overhead slip rings. This output was amplified then passed through a band-pass filter to eliminate unwanted high and low frequencies. The filtered signal was amplified, then clipped and its frequency determined by a counter (Hewlett-Packard, Model 5246L) and printed out. The sample period of the counter was chosen to be either 0·5 s or 1 s depending on the Doppler frequency and the inertial-mode frequency to be resolved. Measurements at different radii and different depths within the cylinder were made by moving the lenses and other optical components and the cylinder itself between experiments. The errors in both the radial and the depth measurement locations were ±0·05 cm.

Between experiments, the water in the cylinder was stirred up about once every hour and its temperature measured. The error in this measurement and the variation in temperature throughout the cylinder were close to ±0·1 °C.

A detailed discussion of the sources of errors for the velocity measurements using this LDV system is given by Fowlis & Martin (1975) and Adrian (1972). The dominant source of systematic errors in the velocity measurements for this work was due to the error in θ. The calculated average value of the standard error in the mean of θ was 0·4%. The error in the radial location of about ±0·05 cm leads to an additional error which is present in the non-dimensional plots of the results (figures 8–16); for $r = 2·37, 4·75$ and 7·12 cm, the errors are ±2·1%, ±1·1% and ±0·7%, respectively. The above error analysis can be checked against the actual experimental results by extrapolating the experimental points in figures 8–16 back to zero time. The observed average spread of about ±2·5% around the expected non-dimensional value of unity is in good agreement with the above analysis.

Random errors are due to the bandwidth of the Doppler signal and the finite sample period. The most important sources of frequency broadening for this work were transit-time broadening and velocity-gradient broadening. The signal-to-noise ratio was always very large and so it was not necessary to consider noise broadening. Transit-time broadening is due to the finite time it takes a scatterer to pass through the cross-over volume of the laser beams and velocity-gradient broadening is due to the radial velocity gradient across the cross-over volume. For these experiments the fractional bandwidths due to transit-time broadening and velocity-gradient broadening were 0·049 and 0·018, respectively. These values combine to give a net fractional bandwidth of 0·052. Using the results of Adrian (1972) for the errors due to zero-crossing counting, we obtain an r.m.s. fluctuation of ±0·4%. Examination of the scatter of the experimental points in figures 8–16 indicates values consistent with this result.

3. The numerical simulations

The simulations were carried out for conditions almost identical to those in the laboratory experiments. The initial flow was taken to be solid-body rotation with

angular velocity Ω_i, then the container's rotation rate was changed impulsively to another value $\Omega_f = \Omega_i \pm \Delta\Omega$ to effect a spin-up or spin-down. The Coriolis term used in the simulations involved this final value Ω_f instead of Ω_i (the value chosen for scaling purposes). This, of course, makes no physical difference but one has to remember what has been done when interpreting some of the results.

The simulations employed finite-difference forms of the axisymmetric incompressible Navier–Stokes equations in cylindrical co-ordinates (r, θ, z) for the respective velocity components (u, v, w). These equations are

$$\frac{\partial u}{\partial t} = -\frac{1}{r}\frac{\partial}{\partial r}(ruu) - \frac{\partial}{\partial z}(uw) + \left(2\Omega_f + \frac{v}{r}\right)v - \frac{1}{\rho}\frac{\partial p}{\partial r} + \nu\left[\frac{\partial}{\partial r}\frac{1}{r}\frac{\partial}{\partial r}(ru) + \frac{\partial^2 u}{\partial z^2}\right], \tag{1}$$

$$\frac{\partial v}{\partial t} = -\frac{1}{r}\frac{\partial}{\partial r}(ruv) - \frac{\partial}{\partial z}(vw) - \left(2\Omega_f + \frac{v}{r}\right)u + \nu\left[\frac{\partial}{\partial r}\frac{1}{r}\frac{\partial}{\partial r}(rv) + \frac{\partial^2 v}{\partial z^2}\right], \tag{2}$$

$$\frac{\partial w}{\partial t} = -\frac{1}{r}\frac{\partial}{\partial r}(ruw) - \frac{\partial}{\partial z}(ww) - \frac{1}{\rho}\frac{\partial p}{\partial z} + \nu\left[\frac{1}{r}\frac{\partial}{\partial r}\left(r\frac{\partial w}{\partial r}\right) + \frac{\partial^2 w}{\partial z^2}\right], \tag{3}$$

where p denotes the pressure and ρ the density. The corresponding continuity equation is

$$\frac{1}{r}\frac{\partial}{\partial r}(ru) + \frac{\partial w}{\partial z} = 0. \tag{4}$$

The initial conditions for the fluid are

$$u = w = 0, \quad v = \pm\Delta\Omega r \quad \text{for} \quad t = 0. \tag{5 a, b}$$

Note that because Ω_f is used in (1) and (2) the plus sign in (5b) denotes a spin-down experiment and the minus sign a spin-up experiment. The boundary conditions on the cylindrical wall and on the bottom and top disks are

$$u = v = w = 0 \quad \text{for} \quad r = b, \quad z = 0, 2h. \tag{6}$$

A thin solid cylinder of very small but finite radius ($r = a$) was inserted to satisfy numerical stability requirements. Symmetry conditions require that

$$u = v = \partial w/\partial r = 0 \quad \text{for} \quad r = a. \tag{7}$$

In order to illustrate the dynamical importance of the thin boundary layers and the corresponding demand that their resolution places on the numerical model, two different grid systems were used: a uniform grid with constant mesh spacing and a stretched grid with variable mesh intervals. The effect of increasing the number of mesh intervals in both cases was observed. Both types are in current use in numerical fluid dynamics, and a comparison of their economy and accuracy seemed to be of interest. The results show that the excessive computer time incurred by the constant-grid code while giving only marginal resolution of the boundary layers makes the stretched-grid code far superior. The results emerging from these experiments indicate that the increased truncation error due to the grid stretching and the poorer resolution of the interior regions do not offset at all the advantages gained by the correct resolution and simulation of the boundary-layer dynamics. The finite differencing of the advection and friction terms was somewhat different in the two cases, but previous numerical experiments have shown the resultant differences to be too small to explain the results with grid stretching and boundary-layer resolution.
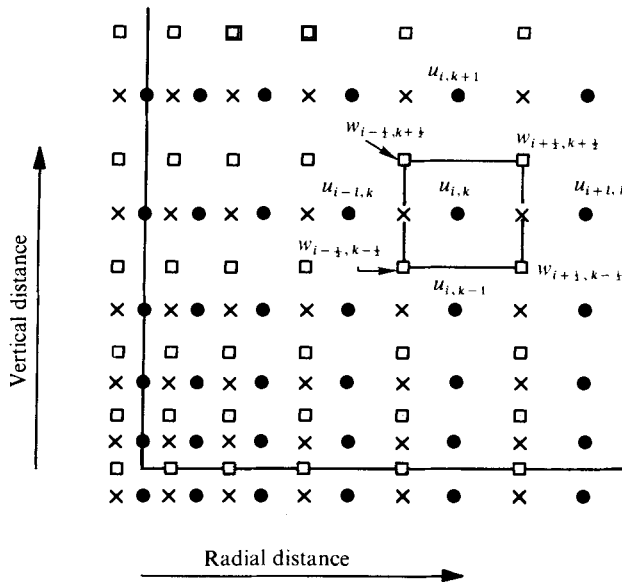
FIGURE 2. The stretched and staggered grid which was used for some of the numerical simulations. This diagram shows qualitatively the variable spacing of the grid points and the staggered arrangement of the points at which the various dependent variables are defined. $\square$, vertical velocity; $\bullet$, radial velocity; $\times$, zonal velocity and pressure.

We shall discuss first the stretching of the mesh and the spatial differencing, then the time differencing and the method used to find the pressure. The stretching of the mesh was accomplished by the use of the function $\xi = [\exp(r/r_l) - 1]/[\exp(r/r_l) + 1]$, where r_l is a normalization constant that controls the stretching in the *l*th boundary layer. For equal increments $\Delta\xi$ of the function $\xi_i = i\Delta\xi$, a set of co-ordinate values r_i will be generated for which $\Delta r = r_i - r_{i-1}$ constitutes the variable mesh spacing. A similar transformation is effected between η and z. It must be pointed out that the equations are not transformed to a new co-ordinate system (ξ, η), but are directly differenced on the new grid (r_i, z_k); the functions ξ and η merely serve the purpose of creating a smoothly varying r, z mesh.

The spatial differencing of all terms in the system (1)–(4) on a constant mesh is performed according to the scheme presented by Williams (1969) and Harlow & Welch (1965), and will not be discussed here. This scheme will be referred to hereafter as scheme A. The difference scheme used on the variable mesh will be referred to as scheme B and will be described below in detail. Bryan (1966) has given an extension of scheme A to variable meshes, but somewhat different procedures will be followed in this paper.

The differencing of the advection terms will be illustrated for the transport part of the radial velocity equation (1). The scheme was presented for constant grids by Piacsek & Williams (1970). We shall denote the co-ordinate axes by r_i and z_k, the time by $t^n = n\Delta t$ and the value of a dependent variable ϕ by $\phi(r_i, z_k; t^n) = \phi_{i,k}^n$, the superscript denoting a time level and the subscripts a mesh-point location in space. Reference should be made to figure 2 to inspect the arrangement of the dependent

variables on the various subsets of the staggered mesh. Using these symbols, we have

$$(4r_i\Delta r_{i+\frac{1}{2}})^{-1}[r_{i+\frac{1}{2}}(u_{i+1}+u_i)u_{i+1}-r_{i-\frac{1}{2}}(u_i+u_{i-1})u_{i-1}]_k$$
$$+(4\Delta z_{k+\frac{1}{2}})^{-1}[(w_{i+\frac{1}{2}}+w_{i-\frac{1}{2}})_{k+\frac{1}{2}}u_{i,k+1}-(w_{i+\frac{1}{2}}+w_{i-\frac{1}{2}})_{k-\frac{1}{2}}u_{i,k-1}]. \quad (8)$$

In the use of staggered meshes, variables that are required at locations where they are not defined are obtained at these points by simple linear averaging. The factor 4 in the denominator of (8) contains a factor of 2 that characterizes the scheme and a factor of 2 that is the result of the simple averaging to find $u_{i+\frac{1}{2},k}$ and $w_{i+\frac{1}{2},k+\frac{1}{2}}$ (see figure 2). In scheme A the quantities $u_{i+1,k}$, $u_{i-1,k}$, $u_{i,k+1}$ and $u_{i,k-1}$ multiplying the brackets are changed to $u_{i+1,k}+u_{i,k}$, $u_{i-1,k}+u_{i,k}$, $u_{i,k}+u_{i,k+1}$ and $u_{i,k-1}+u_{i,k}$, respectively. The advantage of scheme B [i.e. (8)] *vs.* scheme A is that (8) conserves u^2 exactly, whereas scheme A conserves it only when the divergence $\mathcal{D} = \nabla \cdot \mathbf{u}$ vanishes. For a discussion of this point and the method of evaluating conservation properties the reader is referred to Williams (1969) and Piacsek & Williams (1970). It is known that the boundedness of u^2 ensures stability and that of u does not; furthermore, non-zero divergence is always present when iterative methods are used to find the pressure (see subsequent discussion). Thus scheme B has proved superior in most calculations. The remaining terms in (1) are differenced as follows: the pressure term as

$$-\frac{1}{\rho}\frac{1}{\Delta r_{i+\frac{1}{2}}}(p_{i+\frac{1}{2}}-p_{i-\frac{1}{2}})_k; \quad (9)$$

the Coriolis and curvature term as

$$\left[2\Omega_f+\frac{1}{2}\left(\frac{v_{i+\frac{1}{2}}}{r_{i+\frac{1}{2}}}+\frac{v_{i-\frac{1}{2}}}{r_{i-\frac{1}{2}}}\right)\right]_k \frac{1}{2}(v_{i+\frac{1}{2}}+v_{i-\frac{1}{2}})_k; \quad (10)$$

the friction terms as

$$\nu\left\{\frac{1}{\Delta r_{i+\frac{1}{2}}}\left[\frac{1}{r_{i+\frac{1}{2}}}\frac{1}{\Delta r_{i+1}}(r_{i+1}u_{i+1}-r_iu_i)_k-\frac{1}{r_{i-\frac{1}{2}}}\frac{1}{\Delta r_i}(r_iu_i-r_{i-1}u_{i-1})_k\right]\right.$$
$$\left.+\frac{1}{\Delta z_{k+\frac{1}{2}}}\left[\frac{1}{\Delta z_{k+1}}(u_{k+1}-u_k)_i-\frac{1}{\Delta z_k}(u_k-u_{k-1})_i\right]\right\}. \quad (11)$$

The pressure is found from a Poisson equation obtained by taking the divergence of the system (1) and (3). Thus

$$\partial\mathcal{D}/\partial t = -\nabla^2 p + \nabla.\{\mathbf{A}+\mathbf{C}+\mathbf{F}\}, \quad (12)$$

where $\mathbf{A} = (A_u, A_w)$, $\mathbf{C} = (C_u, C_w)$ and $\mathbf{F} = (F_u, F_w)$ are the advection, Coriolis and friction terms in the u and w equations, respectively ($C_w = 0$). The time differencing of the system can be represented using the same notation as

$$(u_l^{n+1}-u_l^{n-1})/2\Delta t = P_l^n + A_l^n + C_l^n + F_l^{n+1,\,n,\,n-1}, \quad (13)$$

where $l = u$, v or w and $F_l^{n+1,\,n,\,n-1}$ is the Dufort–Frankel scheme given by

$$\frac{1}{\Delta\chi_{i+\frac{1}{2}}}\left[\frac{\phi_{i+1}^n-\phi_i^{n+1}}{\Delta\chi_{i+1}}-\frac{\phi_i^{n-1}-\phi_{i-1}}{\Delta\chi_i}\right],$$

where χ is any independent variable. Time differencing (12) yields

$$(\mathcal{D}^{n+1}-\mathcal{D}^{n-1})/2\Delta t = -\nabla^2 p + S^n, \quad (14)$$

where S^n is the second term on the right-hand side of (12). The usual procedure is to set $\mathscr{D}^{n+1} = 0$, but compute the small but non-zero divergence $\mathscr{D}^{n-1}$ due to machine round-off errors and iterate (14) to obtain a pressure which compensates for it in (1) and (3).

The Poisson equation is solved by an ADI iterative approach as

$$\left(r_l - \frac{1}{r}\frac{\partial}{\partial r}r\frac{\partial}{\partial r}\right)p^l_{i,k} = \left(r_l + \frac{\partial^2}{\partial z^2}\right)p^l_{i,k} - S_{i,k},$$

$$\left(r_l - \frac{\partial^2}{\partial z^2}\right)p^{l+1}_{i,k} = \left(r_l + \frac{1}{r}\frac{\partial}{\partial r}r\frac{\partial}{\partial r}\right)p^l_{i,k} - S_{i,k},$$

where the r_l are the iteration parameters, l denoting the iteration number, $p_{i,k}$ is the pressure and $S_{i,k}$ the source term at the grid point (i, k). The continuum second-derivative operators are understood to represent their appropriate finite-difference analogues [as in (11)]. The boundary conditions on the pressure are of the Neumann type, $\partial p/\partial s = G$, where s is the distance normal to the boundary and G is obtained from (13) by applying it on the boundary. The optimum iteration parameters are calculated by the method outlined in Wachpress (1966, p. 194). This method minimizes the maximum eigenvalue of the iteration matrix.

The deviation from second-order accuracy of the space differencing of the non-linear terms will be illustrated for a portion of the vertical velocity equation (13) with $l = w$, namely $\partial w/\partial t = -\partial(ww)/\partial z$. The deviation is given by terms of the form

$$-\frac{1}{2\Delta z_{k+\frac{1}{2}}}(\Delta z^2_{k+1} - \Delta z^2_k)\left[w\frac{\partial^2 w}{\partial z^2} + \frac{1}{2}\left(\frac{\partial w}{\partial z}\right)^2\right],$$

where $\Delta z_{k+1} = z_{k+1} - z_k$, $\Delta z_k = z_k - z_{k-1}$, $\Delta z_{k+\frac{1}{2}} = z_{k+\frac{1}{2}} - z_k$ and the staggering of the grid is as in figure 2. In this case $(\Delta z_k)^2 < |\Delta z_{k+1} - \Delta z_k| < \Delta z_k$ and lies closer to $(\Delta z_k)^2$ than to Δz_k. The formalism thus tends towards second-order accuracy.

The truncation error in the viscous terms is illustrated using part of (1), namely $\partial u/\partial t = \nu\partial^2 u/\partial z^2$, and is

$$+\frac{\nu\Delta t}{\Delta z_{k+\frac{1}{2}}}\frac{\Delta z_{k+1} - \Delta z_k}{\Delta z_k\Delta z_{k+1}}\frac{\partial u}{\partial t} - \frac{\nu\Delta t^2}{2\Delta z_{k+\frac{1}{2}}}\frac{\Delta z_k + \Delta z_{k+1}}{\Delta z_k\Delta z_{k+1}}\frac{\partial^2 u}{\partial t^2} + \text{higher-order terms}.$$

These terms are undesirable and are forced to be small in magnitude through the choice of Δt, Δz_k, $\Delta z_{k+\frac{1}{2}}$ and Δz_{k+1}.

The truncation errors in space and time in these finite-difference equations are usually such that the computed phase advancement of a sinusoidal wave by advection or wave propagation does not equal the true phase advance of the physical phenomenon. This can be readily checked by inserting waves of the form $\exp i(\omega_m n\Delta t + k\Delta z m/L)$ into a linearized form of (13); here $i = (-1)^{\frac{1}{2}}$, ω_m and L/m are the frequency and wavelength of the mth mode, respectively, and $t = n\Delta t$ and $z = k\Delta z$. As an example, we shall investigate the dispersion resulting from the leap-frogging of the Coriolis terms. We shall analyse the following finite-difference equations:

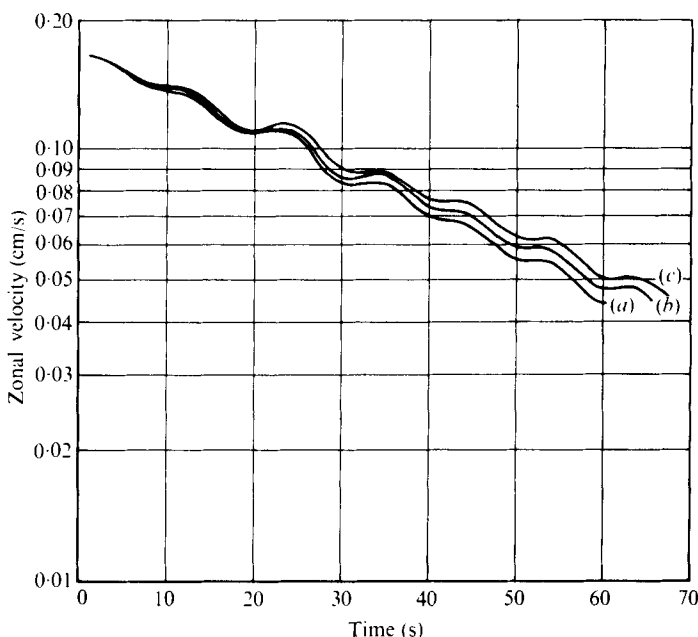$$(u^{n+1} - u^{n-1})/2\Delta t = 2\Omega_f v^n, \quad (v^{n+1} - v^{n-1})/2\Delta t = -2\Omega_f u^n.$$

FIGURE 3. Plots of zonal velocity *vs.* time at the location ($r = 4.75$ cm, $z = 3.00$ cm) for a spin-up simulation in which $\Omega_i = 0.3142$ s^{-1} and $\Delta\Omega = 0.0349$ s^{-1} ($E = 3.30 \times 10^{-3}$, $\epsilon = 0.111$). Curve (*a*) was obtained using scheme *A* on a constant 62×42 grid, curve (*b*) using scheme *A* on a constant 62×82 grid and curve (*c*) on a stretched 42×42 grid.

These equations have the eigenvalues $\lambda = \pm[1 - (\frac{1}{2}\beta)^2] - \mathscr{I}(\frac{1}{2}\beta)$ for $|\beta| < 2$, where $\beta = \Omega_f \Delta t$ and Δt is the time step. The ratio of the computational phase advancement to the true advancement per time step is

$$\frac{\phi}{\phi_0} = \tan^{-1} \pm \frac{-\frac{1}{2}\beta}{\frac{1}{2}[1 - (\frac{1}{2}\beta)^2]^{\frac{1}{2}}\,|\beta|}\,.$$

For a typical spin-up experiment in the range of the experiments described in this paper (see §4), $\Omega_i = 0.6283$ s^{-1}, $\Omega_f = 0.6981$ s^{-1}, $\beta = 4.34 \times 10^{-3}$ and $\phi/\phi_0 \simeq 1 + 2.4 \times 10^{-6}$. The lead in phase of the computational mode is negligible over the $< 10^4$ time steps which were used for the above spin-up. Therefore we do not expect the dispersion effects arising from the finite-difference representation of the Coriolis terms to influence the results significantly.

Restrictions on the time step are due to the finite-differencing of the terms. The nonlinear terms are subject to the Courant–Friedrichs–Lewy condition $\Delta t \leqslant \Delta s/u_0$, where Δs is the smallest grid spacing and u_0 is the largest velocity. The time centring of the Coriolis terms results in a time-step restriction of $\Delta t \leqslant 1/2\Omega$. For the viscous terms the condition $\Delta t/\Delta s < 1$ should be satisfied for the finite-difference equation to correspond to a continuum equation and for the round-off error to be small. The non-physical computational mode which arises from the finite-differencing of the nonlinear terms when a first-order equation in time is raised to a second-order difference equation is eliminated by periodic averaging of the variables.
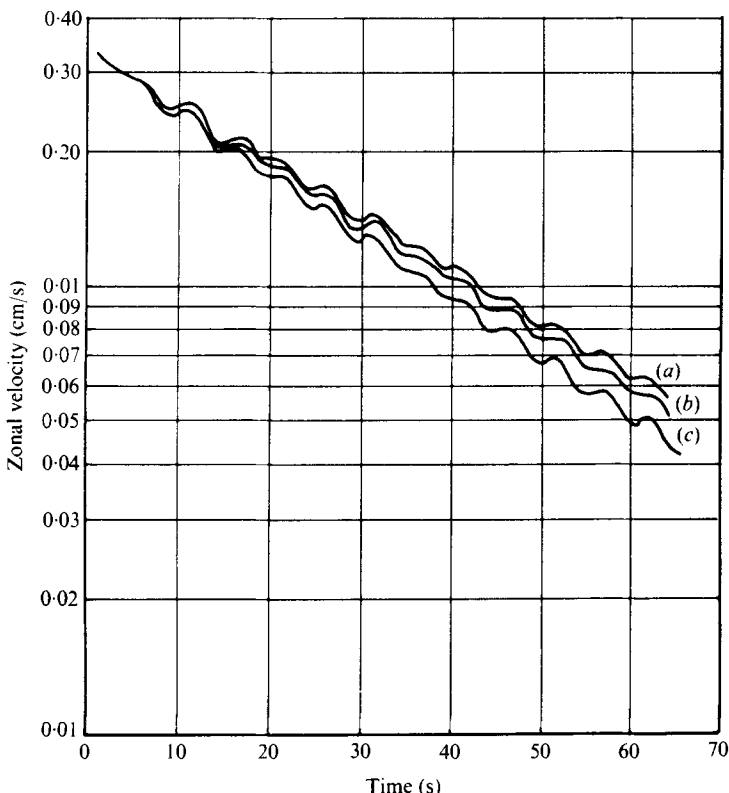
FIGURE 4. Plots of zonal velocity *vs.* time at the location ($r = 4\cdot75$ cm, $z = 3\cdot00$ cm) for a spin-down simulation in which $\Omega_i = 0\cdot6981$ s^{-1} and $\Delta\Omega = 0\cdot0698$ s^{-1} ($E = 1\cdot49 \times 10^{-3}$, $\epsilon = 0\cdot200$). All three curves were obtained using scheme B on a stretched grid. Curve (a) was obtained with an 82×82 grid and curves (b) and (c) with a 42×42 grid.

Ekman-layer resolution

The number of grid points in the Ekman layer required to stabilize the spin-up and spin-down times, i.e. lead to convergent results, was determined by performing a series of numerical simulations using schemes A and B on grids with different numbers of points in the Ekman-layer region. The parameters chosen for these tests were the same as those for the laboratory experiment whose results are presented in figure 8(a), namely $\Omega_i = 0\cdot3142$ s^{-1}, $\Delta\Omega = +0\cdot0349$ s^{-1}, $E = 3\cdot30 \times 10^{-3}$ and $\epsilon = 0\cdot111$. Using scheme A the equations were first solved on a 62×42 constant grid

$$(\Delta r = 0\cdot158 \text{ cm}, \quad \Delta z = 0\cdot150 \text{ cm}).$$

The results for the zonal velocity as a function of time for the midradius ($r = 4\cdot75$ cm) and middepth ($z = 3\cdot00$ cm) location are shown in figure 3 as curve (a). Then the number of mesh intervals in the vertical was doubled ($\Delta z = 0\cdot075$ cm) and the equations solved again. The results for the zonal velocity for the location ($r = 4\cdot75$ cm, $z = 3\cdot00$ cm) are shown in figure 3 as curve (b). This grid-point density corresponds to one grid point in the rising portion of the radial velocity profile of the Ekman layer. Further experiments using scheme A with increased vertical resolution were not performed because of the excessive computer time they would have required.
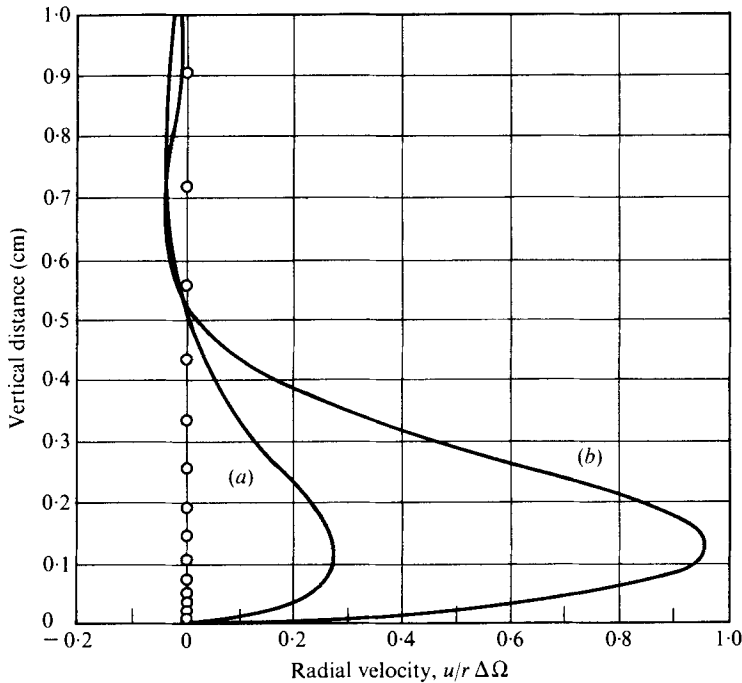
FIGURE 5. (a) Radial velocity profile of the bottom Ekman layer for the spin-up simulation of figure 3, curve (c) for $r = 4.75$ cm and a time of 0.278 rotations after the impulsive start. (b) Radial velocity profile of the Ekman layer obtained from the linearized, steady-state theory for the same parameters as curve (a).

Next scheme B was used on a stretched 42×42 grid. The stretching of the grid enabled us to place enough grid points in the Ekman layer to make the spin-up times converge without increasing the total number of mesh points and the corresponding computer time. The spin-up times stabilized for a resolution which had six grid points in the rising portion of the radial velocity profile in the Ekman layer. This was taken to be our asymptotic numerical solution. The decay curve for the six-point resolution is shown in figure 3 as curve (c). The side-wall boundary layers were resolved by stretching the grid in the radial direction. The thinnest of the side-wall boundary layers, the so-called Stewartson layer, whose thickness is given by $E^{\frac{1}{3}} \times h = 0.447$ cm, was resolved by approximately nine grid points.

Simulations were also carried out using scheme B on stretched grids with 42×42 and 82×82 points for a spin-down from 0.6981 s^{-1} to 0.6283 s^{-1}. In the case of the 82×82 grid we had a better overall resolution, particularly in the interior region, and had seven points in the rising portion of the radial velocity profile in the Ekman layer. We were thus able to observe the effects of halving the spatial truncation terms. In the case of the 42×42 grid three stretchings were tried, with one, three and six grid points in the rising portion of the Ekman layer. Figure 4 shows the results of these experiments. Curve (a) represents the simulation with the 82×82 grid; this is identical to the one obtained with the 42×42 grid with six points in the boundary layer. Curves (b) and (c) are for the three- and one-point boundary-layer resolution, respectively. We have thus established our asymptotic limit on the spin-down time of the simulations.
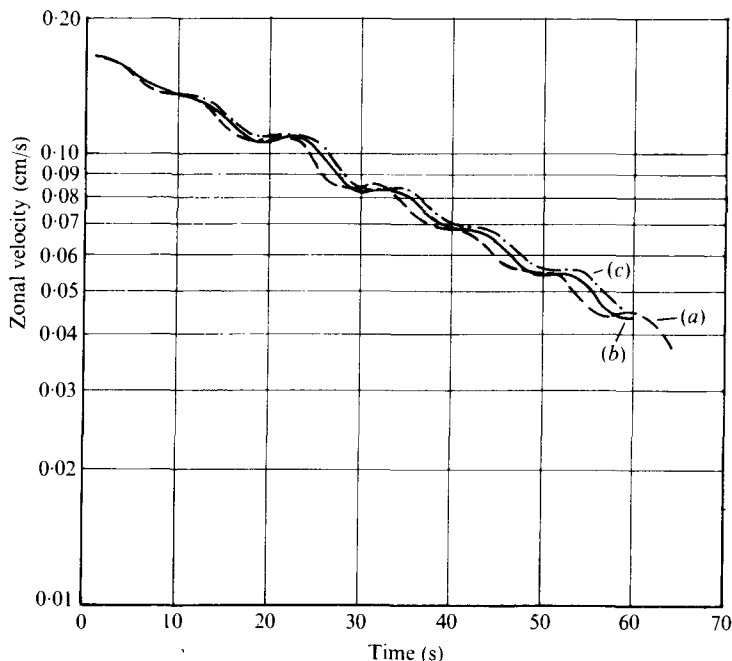
FIGURE 6. Plots of zonal velocity *vs.* time at the location ($r = 4.75$ cm, $z = 3.00$ cm) for a spin-up simulation in which $\Omega_i = 0.3142$ s^{-1} and $\Delta\Omega = 0.0349$ s^{-1} ($E = 3.30 \times 10^{-3}$, $\epsilon = 0.111$). All three curves were obtained using scheme A on a constant 62×42 grid. Curve (a) is for the linearized simulation, curve (b) for a linearized simulation in which the nonlinear curvature terms were included and curve (c) for the nonlinear simulation.

In order to show clearly what has been resolved, the radial velocity in the Ekman layer was plotted from the numerical results for the simulation of figure 3, curve (c). Figure 5 shows the flow profile for the midradius ($r = 4.75$ cm) at a time of 0.278 rotations after the impulsive start. The locations of the grid points are also shown. For comparison, the dimensionless, linearized, steady-state, analytical solution (Greenspan 1969, p. 31), namely

$$u = r \exp(-E^{-\frac{1}{2}}z) \sin E^{-\frac{1}{2}}z,$$

is also shown for the same values of the dimensionless parameters. The curves in figure 5 show almost exact agreement in the locations of the first maximum and the first zero away from the boundary. An Ekman-layer thickness can be defined as $E^{\frac{1}{2}}h$, which for the parameters of figure 5 is 0.149 cm. Another definition of the thickness is the distance at which the analytical solution has its first zero away from the boundary, namely $z = \pi E^{\frac{1}{2}}h$, which for the parameters of figure 5 is 0.468 cm. Note the six grid points within the rising portion of the flow profile between the wall and the first maximum.

The nonlinear terms

The effects of the nonlinear terms were investigated by omitting these terms in a numerical simulation and comparing the results with the corresponding nonlinear simulation. Using scheme A on a constant 62×42 grid, an experiment was performed for spin-up from 0.3142 s^{-1} to 0.3491 s^{-1}. The other parameters were the same as those for the laboratory experiment whose results are presented in figure 8(a). The
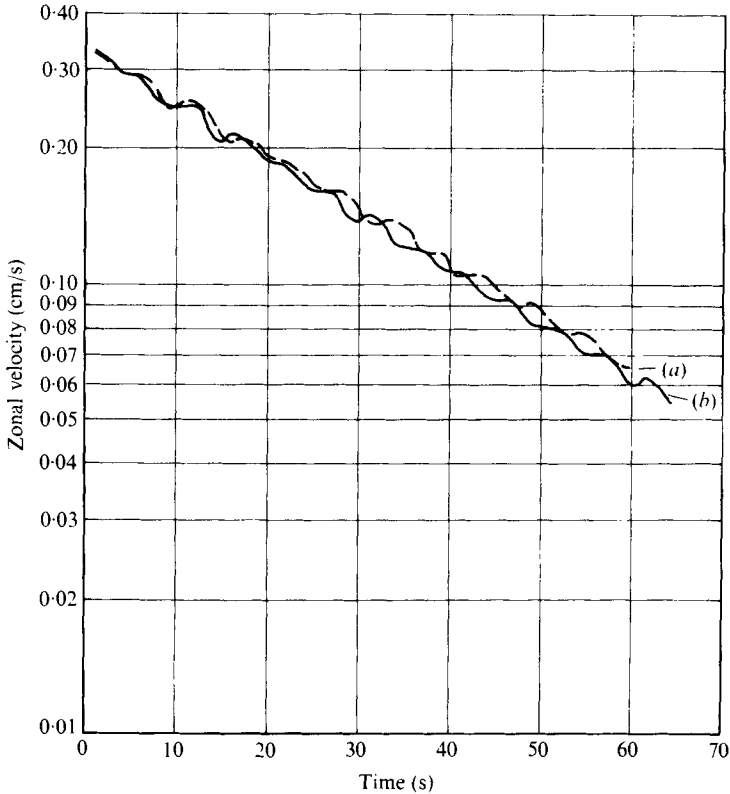
FIGURE 7. Plots of zonal velocity *vs.* time at the location ($r = 4\cdot75$ cm, $z = 3\cdot00$ cm) for a spin-down simulation in which $\Omega_i = 0\cdot6981$ s^{-1} and $\Delta\Omega = 0\cdot0698$ s^{-1} ($E = 1\cdot49 \times 10^{-3}$, $\epsilon = 0\cdot100$). Both curves were obtained using scheme B on a stretched 42×42 grid. Curve (a) is for the linearized simulation and curve (b) is for the nonlinear simulation.

results for the zonal velocity at the location ($r = 4\cdot75$ cm, $z = 3\cdot00$ cm) are shown in figure 6: curve (a) is for the linearized simulation, curve (b) is for a linearized simulation in which the nonlinear curvature terms were included and curve (c) is for the nonlinear simulation. The Rossby number for these simulations is $0\cdot111$. A larger Rossby number should have been used but such simulations were not performed. However, the effects of nonlinearity are observed with the existing results. A comparison of the inertial frequencies shows that only the curvature terms significantly affect the frequency, and that the inertial frequency in the linear case is greater than that in the nonlinear case. This frequency difference is explained as follows. The relationship between inertial-mode frequencies and the basic rotation rate is given by (15) (see § 5). This relationship states that a decrease in Ω means a decrease in frequency. The Coriolis term in the governing equations (1) and (2) involves $2\Omega_f$ and when the curvature terms are included the effective Coriolis term involves $2\Omega_f + v/r$. For the experiment with spin-up from Ω_i to Ω_f, v was initially set equal to $-\Delta\Omega r$. This effectively decreases the rotation rate for the nonlinear case compared with the linear case and hence the frequency in the linear case is greater than that in the nonlinear case. As the fluid spins up and v decays, the frequency in the nonlinear case will approach that of the linearized case.
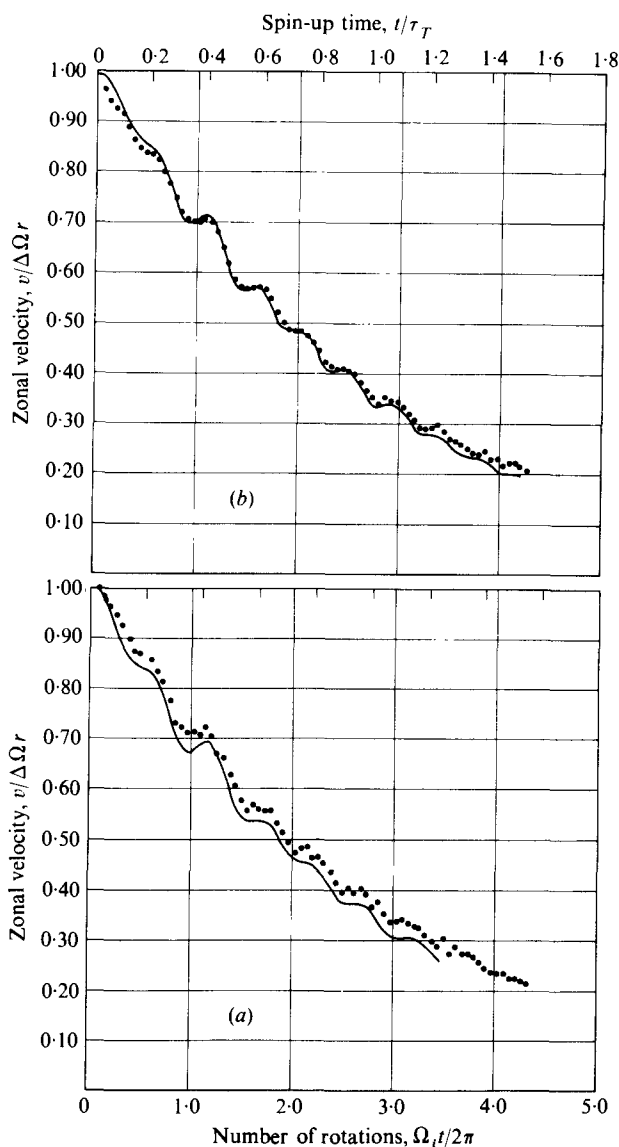
FIGURE 8. Spin-up results for the location ($r = 4.75$ cm, $z = 3.00$ cm). ●, experimental measurements; ——, numerical solutions. (a) Results for $E = 3.30 \times 10^{-3}$ and $\epsilon = +0.111$. (b) Results for $E = 3.30 \times 10^{-3}$ and $\epsilon = +0.333$. For further details see table 1.

Using scheme B on a variable 42×42 grid, an experiment with spin-down from 0.6981 s^{-1} to 0.6283 s^{-1} was performed. The other parameters were the same as those for the laboratory experiment whose results are presented in figure 12. The results for the zonal velocity at the location ($r = 4.75$ cm, $z = 3.00$ cm) are shown in figure 7: curve (a) is for the linearized simulation and curve (b) for the nonlinear simulation. Note that this time the frequency in the linear case is smaller than that in the nonlinear case. This result is consistent with the above argument.
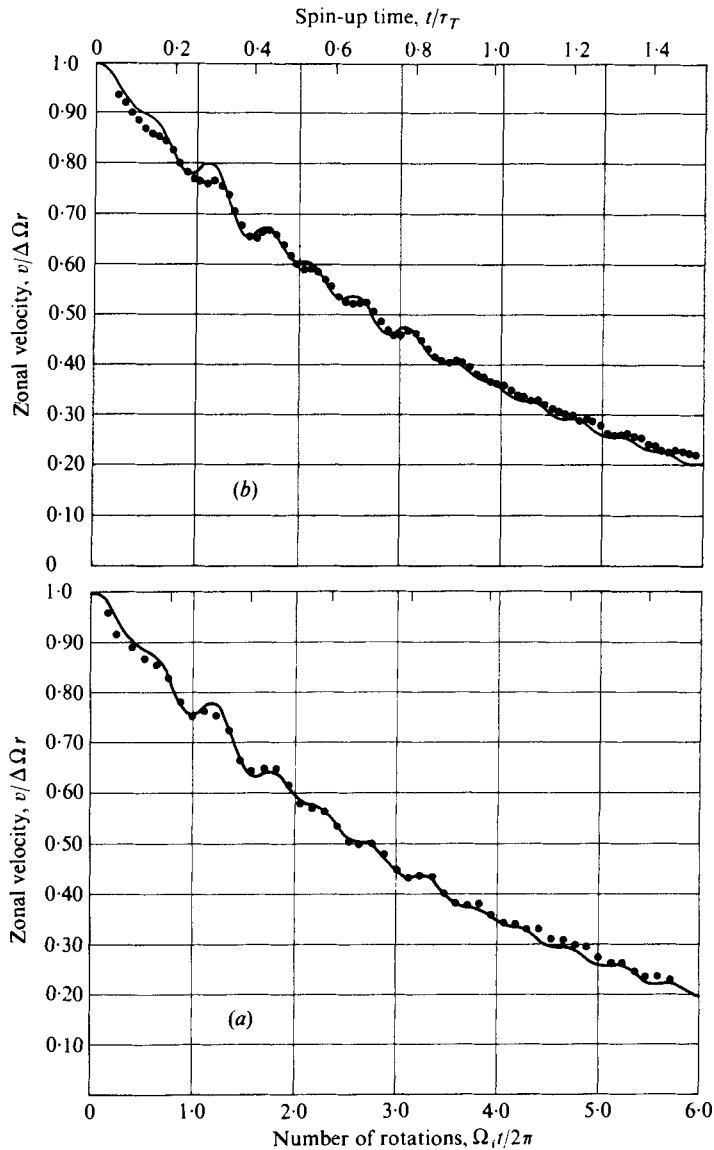
FIGURE 9. Spin-up results for the location ($r = 4.75$ cm, $z = 3.00$ cm). (a) Results for $E = 1.65 \times 10^{-3}$ and $\epsilon = +0.111$. (b) Results for $E = 1.58 \times 10^{-3}$ and $\epsilon = +0.333$. For further details see table 1.

4. The results

The results of a selection from the laboratory experiments and the numerical simulations carried out over a range of values of E and ϵ and for different values of r and z are presented in this section. The experiments were performed as described in § 2. The simulations were performed using scheme B on a stretched grid with a stretching which placed six grid points in the rising portion of the radial velocity profile of the Ekman layer as described in § 3. The experimental and numerical
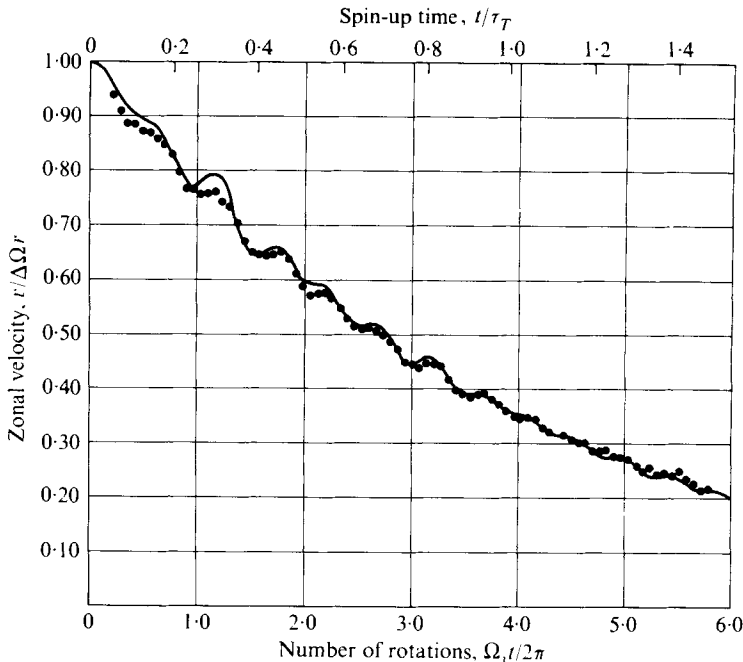
FIGURE 10. Spin-up results for the location ($r = 4\cdot75$ cm, $z = 3\cdot00$ cm) for $E = 1\cdot67 \times 10^{-3}$ and $\epsilon = +0\cdot222$. For further details see table 1.

results are shown and compared in figures 8–16. They are displayed as plots of the non-dimensional zonal velocity $v/\Delta\Omega r$ vs. the non-dimensional time $\Omega_i t/2\pi$ (i.e. the number of rotations based on Ω_i). The upper abscissa shows the non-dimensional spin-up time $(\nu\Omega_i)^{\frac12}t/h$ based on linear theory (Greenspan & Howard 1963). The results are plotted to show the decay of a positive velocity for both spin-up and spin-down experiments. The dots are the experimental measurements and the continuous curves are the numerical results.

The laboratory experiments and the numerical simulations were not carried out for identical conditions; several small differences did exist. For the simulations the change in rotation rate was effectively instantaneous but for the experiments there were the small time delays discussed in § 2. The values of ν were not always identical; however, the differences between the numerical and experimental values ranged from less than 1 % to a maximum of 2·7 %. For the experiments $2h$ was 6·04 cm and for the simulations it was 6·00 cm. The simulations were carried out with a small inner cylinder of radius 0·01 cm; an increase of this radius to 0·1 cm showed no difference in the results.

Figures 8–11 show spin-up results for the midradius ($r = 4\cdot75$ cm) and middepth ($z = 3\cdot00$ cm) location and various values of Ω_i and $\Delta\Omega$. Figures 8 (a) and (b) show the results of two experiments and simulations for $\Omega_i = 0\cdot3142$ s^{-1} (rotation period = 20·00 s) and $\Delta\Omega = +0\cdot0349$ s^{-1} and $+0\cdot1047$ s^{-1}, respectively. For these experiments table 1 gives the values of Ω_i and $\Delta\Omega$ and also the values of the final rotation rate Ω_f and the non-dimensional parameters E and ϵ. The values of the water temperature T, the kinematic viscosity ν and the sample period p for the laboratory experiments are also given. A plus sign in front of $\Delta\Omega$ and ϵ is used to denote a spin-up experiment and
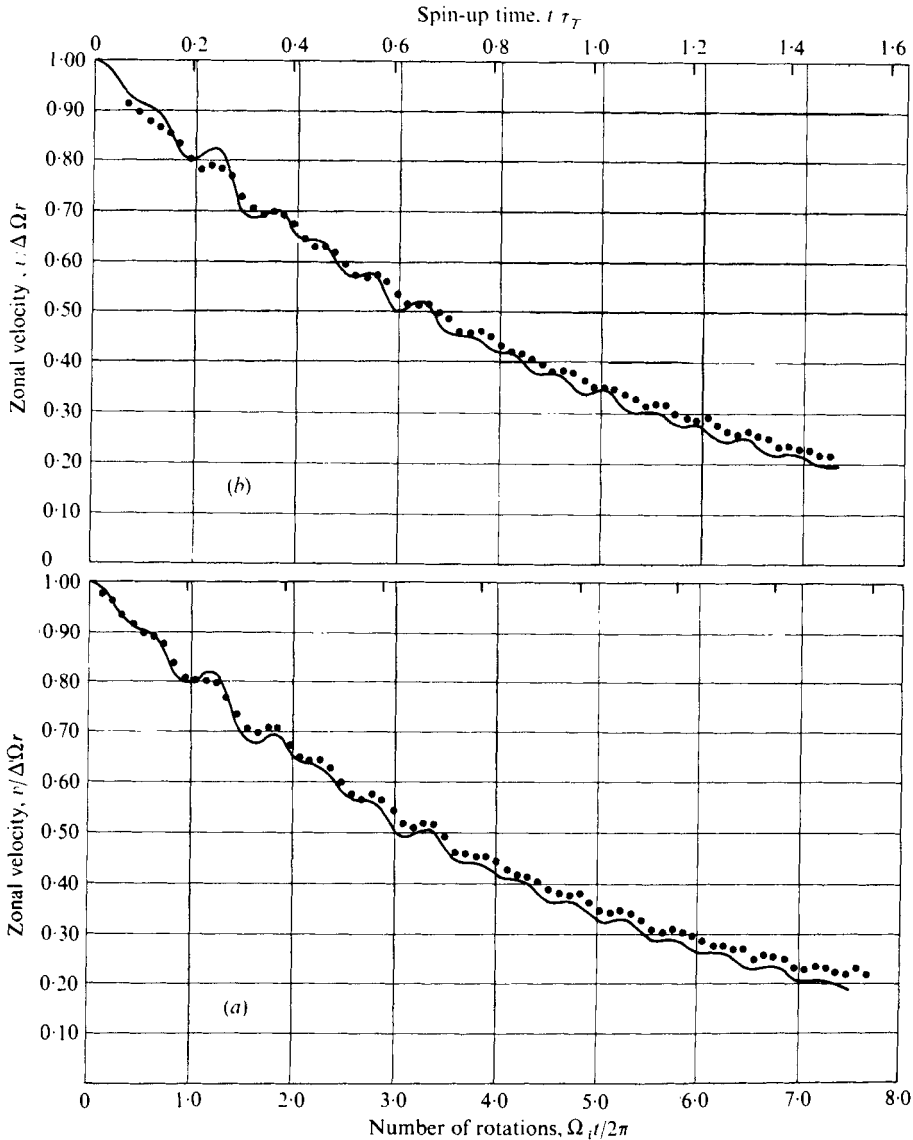
FIGURE 11. Spin-up results for the location ($r = 4.75$ cm, $z = 3.00$ cm). (a) Results for $E = 1.10 \times 10^{-3}$ and $\epsilon = +0.111$. (b) Results for $E = 1.06 \times 10^{-3}$ and $\epsilon = +0.222$. For further details see table 1.

a minus sign to denote a spin-down experiment. Figures 9 (a) and (b) show the results of two experiments and simulations for $\Omega_i = 0.6283$ s^{-1} (rotation period $= 10.00$ s) and $\Delta\Omega = +0.0698$ s^{-1} and $+0.2094$ s^{-1}, respectively. Figure 10 also shows results for $\Omega_i = 0.6283$ s^{-1} but for the intermediate value $\Delta\Omega = +0.1396$ s^{-1}. The values of the other parameters are again given in table 1. Figures 11 (a) and (b) show the results of two experiments and simulations for $\Omega_i = 0.9425$ s^{-1} (rotation period $= 6.667$ s) and $\Delta\Omega = +0.1047$ s^{-1} and $+0.2094$ s^{-1}, respectively, with the values of the other parameters given in table 1.

Figure number	Ω_i (s⁻¹)	Ω_f (s⁻¹)	$\Delta\Omega$ (s⁻¹)	T (°C)	$\nu \times 10^2$ (cm² s⁻¹)	p (s)	$E \times 10^3$	ϵ
8(a)	0·3142	0·3491	+0·0349	22·5	0·948	1	3·30	+0·111
8(b)	0·3142	0·4189	+0·1047	22·5	0·948	1	3·30	+0·333
9(a)	0·6283	0·6981	+0·0698	22·5	0·948	1	1·65	+0·111
10	0·6283	0·7679	+0·1396	22·3	0·953	0·5	1·67	+0·222
9(b)	0·6283	0·8378	+0·2094	24·25	0·910	0·5	1·58	+0·333
11(a)	0·9425	1·0472	+0·1047	22·65	0·945	0·5	1·10	+0·111
11(b)	0·9425	1·1519	+0·2094	24·35	0·908	0·5	1·06	+0·222
12	0·6981	0·6283	−0·0698	22·5	0·948	0·5	1·49	−0·200

TABLE 1. Values of the parameters for the laboratory experiments and numerical simulations in which Ω_i and $\Delta\Omega$ alone were varied. The location was at the midradius and middepth ($r = 4·75$ cm, $z = 3·00$ cm). Specific experiments and simulations are identified by the figure number in which the results are presented.

Figure number	r (cm)	z (cm)	T (°C)	$\nu \times 10^2$ (cm² s⁻¹)	p (s)	$E \times 10^3$
13(a)	2·37	0·75	22·65	0·945	0·5	1·66
13(b)	2·37	3·00	22·75	0·943	0·5	1·64
14(a)	2·37	4·50	22·75	0·943	0·5	1·64
14(b)	2·37	5·25	22·80	0·942	0·5	1·64
15(a)	4·75	0·75	22·6	0·946	0·5	1·65
15(b)	4·75	3·00	22·6	0·946	0·5	1·65
16(a)	7·12	0·75	22·9	0·940	0·5	1·64
16(b)	7·12	3·00	22·9	0·940	0·5	1·64

TABLE 2. Values of the parameters for the laboratory experiments and numerical simulations in which the location alone was varied. The values of Ω_i, $\Delta\Omega$ and ϵ were 0·6283 s⁻¹, +0·1396 s⁻¹ and +0·222, respectively, and the values of E were as shown. Specific experiments and simulations are identified by the figure number in which the results are presented.

Figure 12 shows the results of a spin-down experiment and simulations for $r = 4·75$ cm, $z = 3·00$ cm, $\Omega_i = 0·6981$ (rotation period = 9·000 s) and $\Delta\Omega = -0·0698$ s⁻¹. The values of the other quantities are given in table 1.

Figures 13–16 show spin-up results for fixed values of Ω_i and $\Delta\Omega$ and variable r and z. These experiments and simulations were carried out for $\Omega_i = 0·6283$ s⁻¹ (rotation period = 10·00 s) and $\Delta\Omega = +0·1396$ s⁻¹ and hence for $\epsilon = +0·222$. Figures 13(a), 13(b), 14(a) and 14(b) show the results of four experiments and simulations for $r = 2·37$ cm and $z = 0·75$ cm, 3·00 cm, 4·50 cm and 5·25 cm, respectively. The values of r, z, T, ν, p and E are given in table 2. Because of the symmetry of the experimental set-up about the middepth plane ($z = 3·00$ cm) the results shown in figures 12(a) and 13(b) for $z = 0·75$ cm and 5·25 cm should be identical within the experimental tolerance (see §2). Figures 15(a) and (b) show the results of two experiments and simulations for $r = 4·75$ cm and $z = 0·75$ cm and 3·00 cm, respectively. The values of the other quantities are given in table 2. The reproducibility of the experiments is demonstrated by comparing figure 15(b) with figure 10 since these results are for almost identical values of all the parameters. Figures 16(a) and (b)
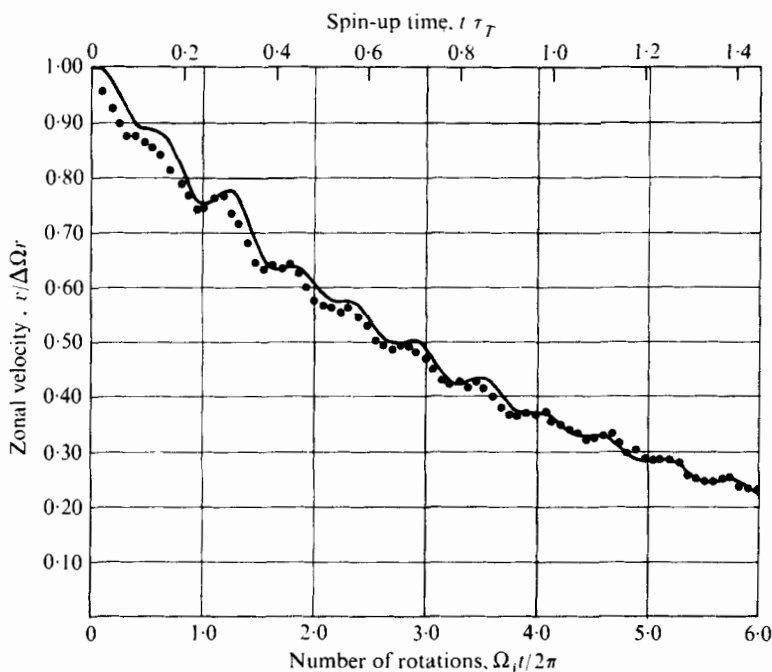
FIGURE 12. Spin-down results for the location ($r = 4\cdot75$ cm, $z = 3\cdot00$ cm) for $E = 1\cdot49 \times 10^{-3}$ and $\epsilon = -0\cdot200$. For further details see table 1.

show the results of two experiments and simulations for $r = 7\cdot12$ cm and $z = 0\cdot75$ cm and $3\cdot00$ cm, respectively. The values of the other quantities are given in table 2.

5. Analysis and discussion of the results

All the comparisons between the numerical and the experimental results shown in figures 8–16 show good agreement. After four, and sometimes seven, rotation periods the agreement is still good. All systematic upward or downward displacements of the results with respect to one another are within the experimental tolerance discussed in §2. In general the results agree to within a few per cent. The agreement is good not only for the overall decay of the zonal flow but also for the amplitudes and phases of the weakly excited inertial modes. Only the results shown in figure 8(a) indicate a deviation which is a little greater than the experimental tolerance. This good agreement means that the small differences between the simulations and the experiments (see §4) did not produce significant differences in the results. Particularly noteworthy in this context is the absence of a noticeable effect due to the small time delays in changing the rotation rate of the turntable (see §2).

The dimensional angular frequencies of the linearized, inviscid, axisymmetric, inertial modes in a homogeneous cylinder of fluid are given by (Greenspan 1969, p. 83)
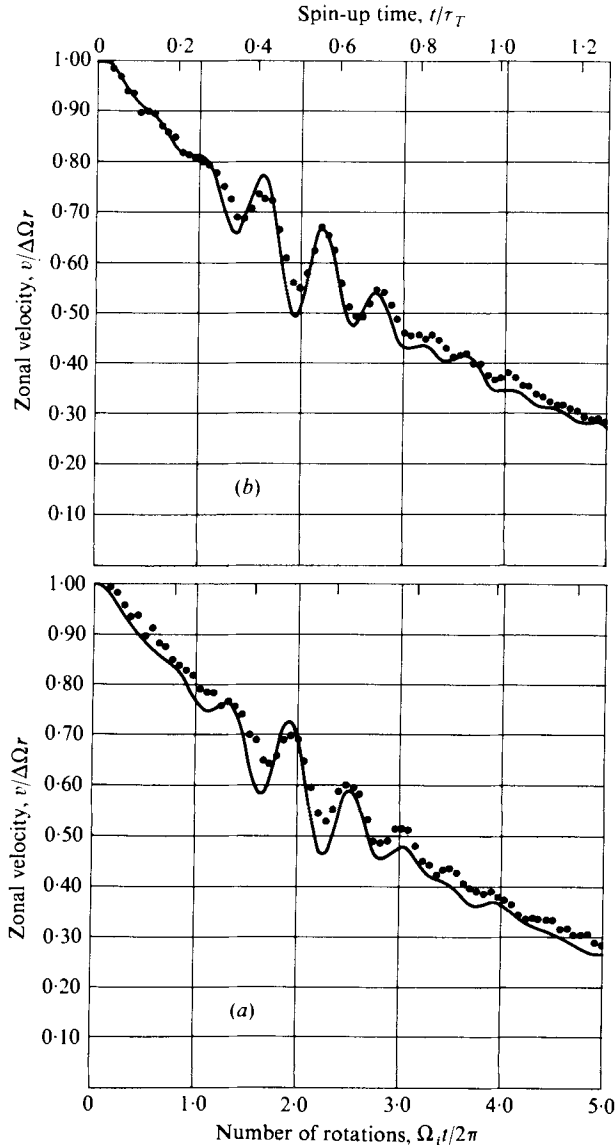
$$\sigma = 2\Omega[1 + 4\gamma_n^2 h^2/\pi^2 m^2 b^2]^{-\frac{1}{2}}, \tag{15}$$

FIGURE 13. Spin-up results for $E = 1 \cdot 65 \times 10^{-3}$ and $\epsilon = +0 \cdot 222$. ●, experimental measurements; ——, numerical solutions. (a) Results for the location ($r = 2 \cdot 37$ cm, $z = 0 \cdot 75$ cm). (b) Results for the location ($r = 2 \cdot 37$ cm, $z = 3 \cdot 00$ cm). For further details see table 2.

where the γ_n are the zeros of first-order Bessel functions and m is any integer. Previous experimental results (Fowlis & Martin 1975) showed that all the detectable energy was present at the frequency corresponding to the $m = 2$, $n = 1$ mode. This is the mode which is symmetrical about the middepth plane and has the gravest structure in the radial direction. The non-dimensional period of this mode, in terms of the rotational period, is $0 \cdot 536$. The results show that this mode grows in amplitude for about $1\frac{1}{2}$ rotation periods before starting to decay. The time scale for the decay of the mode is closer to $E^{\frac{1}{2}}$ than E as predicted by Greenspan & Howard (1969) for a
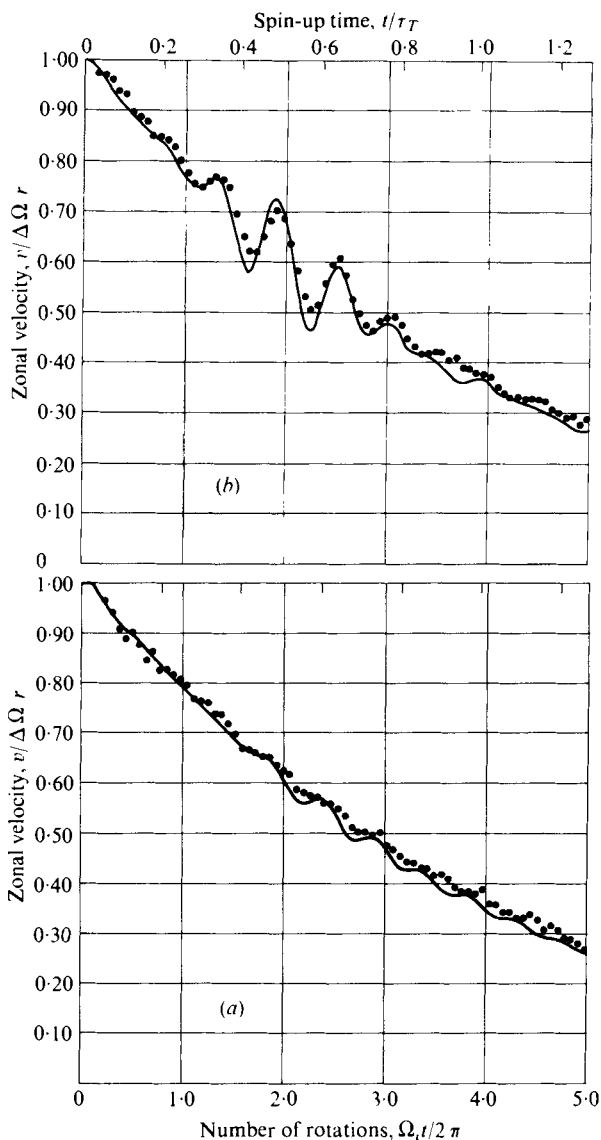
FIGURE 14. Spin-up results for $E = 1.64 \times 10^{-3}$ and $\epsilon = +0.222$. (a) Results for the location ($r = 2.37$ cm, $z = 4.50$ cm). (b) Results for the location ($r = 2.37$ cm, $z = 5.25$ cm). For further details see table 2.

finite cylindrical geometry. The results presented in this paper essentially confirm the previous conclusion except that some of the results show a weak, longer time scale variation of amplitude which is suggestive of beating and implies the presence of another mode of a similar period. This is most obvious for the results for higher rotation rates in figures 11 (a) and (b).

The spin-up results presented in figures 8–11 show that, for a given E and ϵ, the period of the inertial mode decreases with time and that for a given E, as ϵ increases, this decrease becomes larger. The opposite effect is apparent for the spin-down result
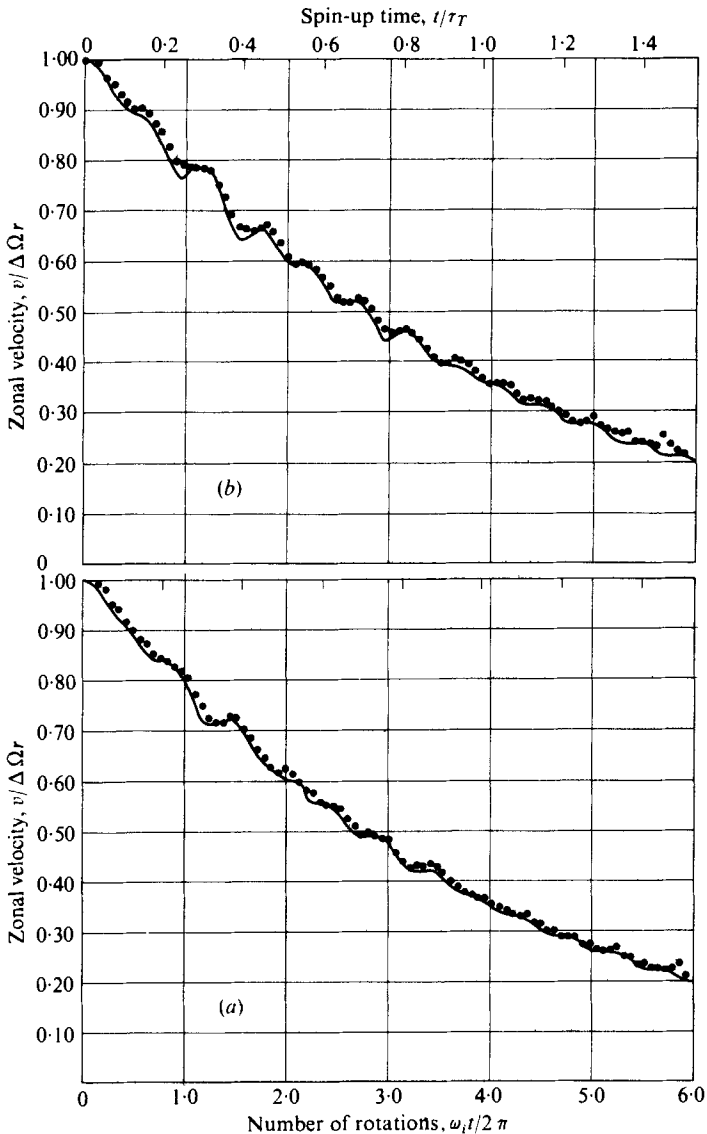
FIGURE 15. Spin-up results for $E = 1.65 \times 10^{-3}$ and $\epsilon = +0.222$. (a) Results for the location ($r = 4.75$ cm, $z = 0.75$ cm). (b) Results for the location ($r = 4.75$ cm, $z = 3.00$ cm). For further details see table 2.

in figure 12. This result can be understood from (15): as the fluid spins up (spins down), the effective interior value of Ω increases (decreases) and the angular frequency of the mode also increases (decreases).

The spatial structure of the mode can be examined from the variable r and z results shown in figures 13–16. Note the antinode with relatively large amplitude for $z = 3.00$ cm in figures 13(b), 15(b) and 16(b) and the node with reduced amplitude for $z = 4.50$ cm in figure 14(a). Note also that the oscillations for $z = 0.75$ and 5.25 cm
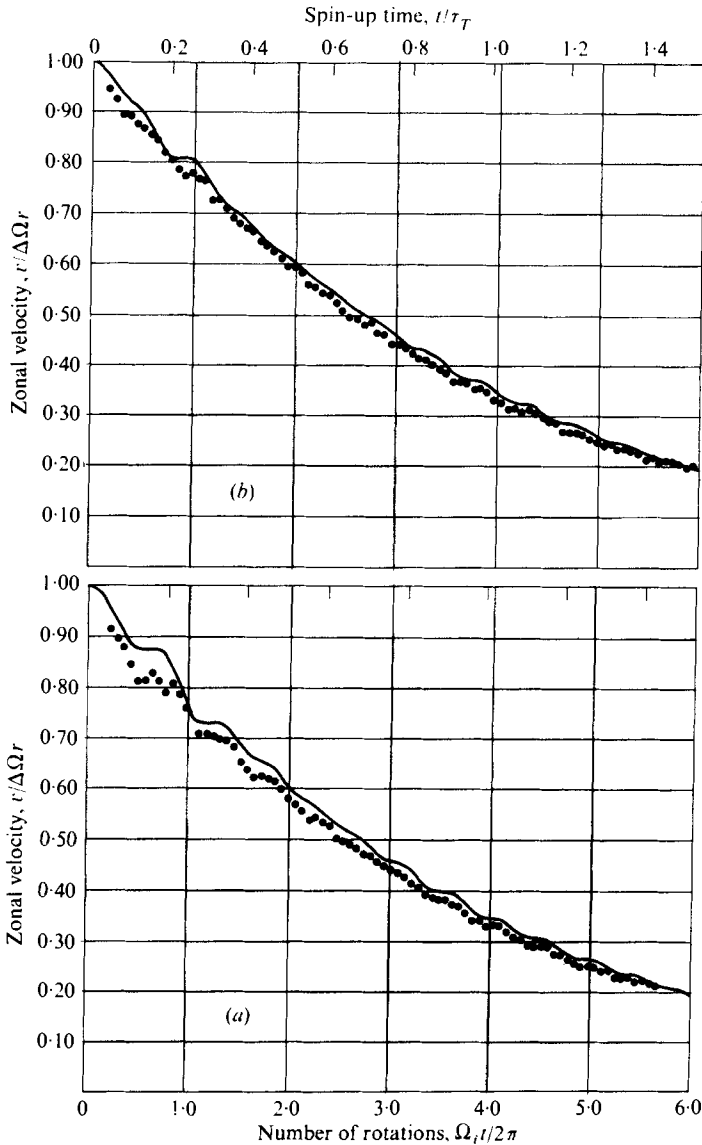
FIGURE 16. Spin-up results for $E = 1.64 \times 10^{-3}$ and $\epsilon = +0.222$. (a) Results for the location $(r = 7.12 \text{ cm}, z = 0.75 \text{ cm})$. (b) Results for the location $(r = 7.12 \text{ cm}, z = 3.00 \text{ cm})$. For further details see table 2.

are out of phase with those at 3.00 cm. For a given z the amplitude of the mode is relatively larger at small radii than at large radii. This result is not consistent with the simple inviscid eigenvalue problem (Greenspan 1969, p. 82), which gives a first-order Bessel function for the amplitude in the radial direction.

Plots of the meridional stream function for conditions similar to those of figure $8(a)$ $(\Omega_i = 0.3142 \text{ s}^{-1}, \Delta\Omega = +0.0349 \text{ s}^{-1}, E = 3.30 \times 10^{-3}, \epsilon = +0.111)$ were obtained from the numerical solution. Figure 17 shows the stream function for dimensionless times (rotation periods) after the impulsive start of 0.65, 0.85, 1.05 and 1.28, respectively. These plots were obtained using scheme A on a 62×42 constant mesh
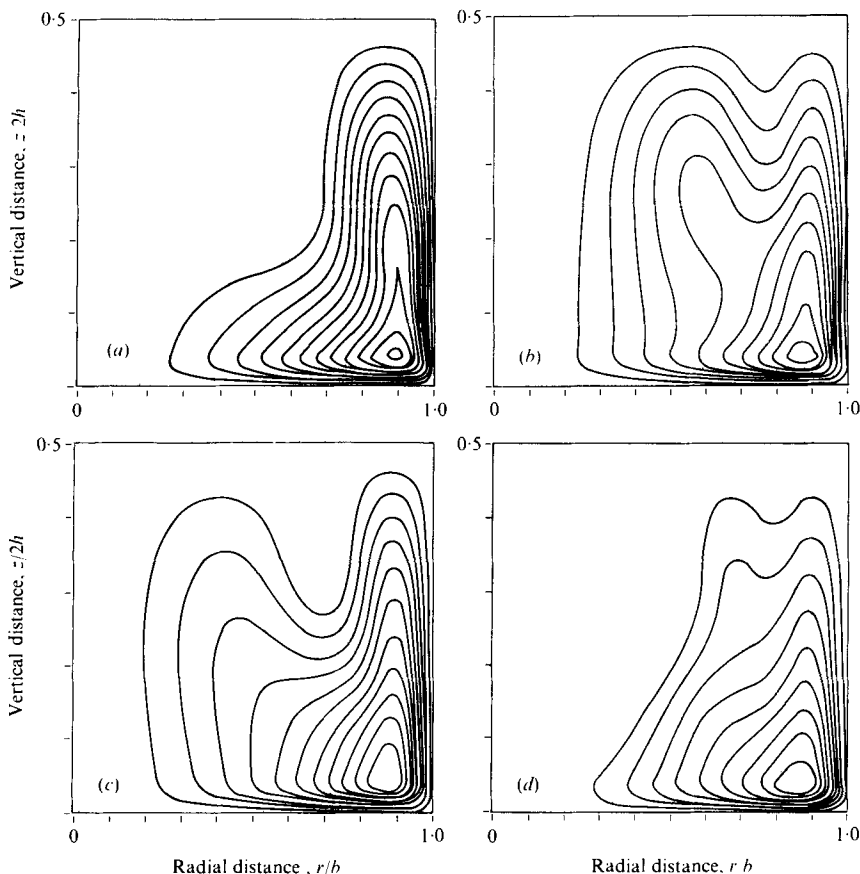
FIGURE 17. Stream-function contours for a spin-up simulation for values of the parameters identical to those for the results in figure 8(a) ($E = 3\cdot30 \times 10^{-3}$, $\epsilon = +0\cdot111$). Number of rotations after the impulsive start: (a) 0·65, (b) 0·85, (c) 1·05, (d) 1·28. These contours were obtained using scheme A on a constant 62×42 grid.

whereas the numerical results shown in figure 8(a) were obtained using scheme B on a stretched grid (see §4); the former method, however, is satisfactory for qualitative examination of the essential features of the meridional flow. The plots show a combination of the spin-up flow and the inertial-mode flow. Note the flux of fluid in the Ekman layer and the side-wall boundary layer. The observed strong oscillation of the interior flow at the inertial-mode period tells us that the spin-up part and the inertial part are comparable in amplitude.

Analytical results for conditions identical to the laboratory experiments and numerical simulations are not available. However it is still informative to make comparisons and in what follows some similar linear and nonlinear theories are compared with the laboratory results. Greenspan & Howard (1963, referred to below as G & H) carried out a linearized analysis ($\epsilon \ll E^{\frac{1}{2}} \ll 1$) for spin-up between two infinite parallel disks which included the inertial oscillations. Note that for the experiments

$$0\cdot033 \leqslant E^{\frac{1}{2}} \leqslant 0\cdot057 \quad \text{and} \quad 0\cdot100 \leqslant |\epsilon| \leqslant 0\cdot333,$$
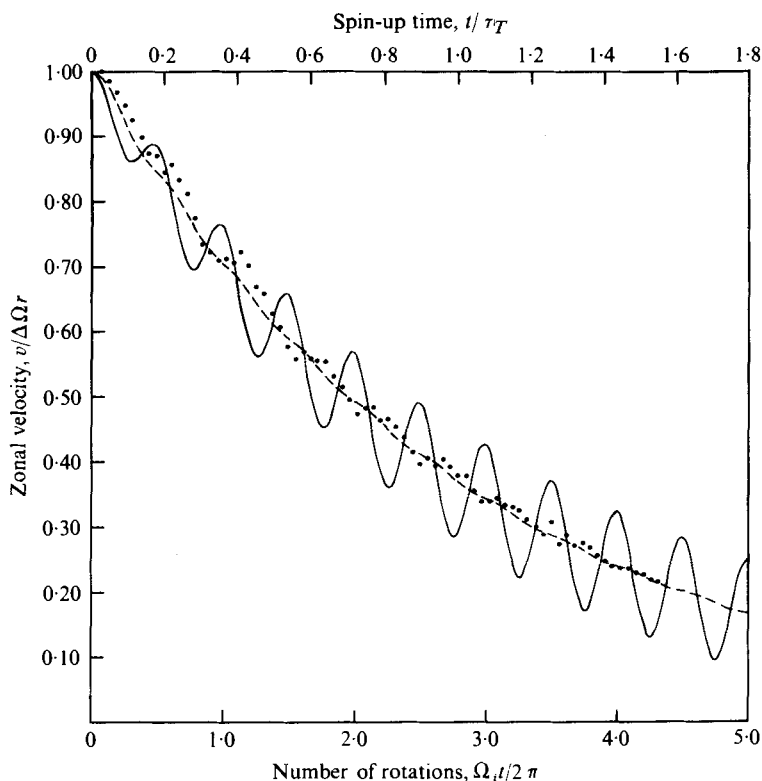
FIGURE 18. Comparison of the experimental results in figure 8(a) ($E = 3\cdot30 \times 10^{-3}$ and $\epsilon = +0\cdot111$) with the analytical results of Greenspan. & Howard (1963). $\cdots$, experimental results; ———, theory, equation (17); ———, theory, equation (18).

thus it might appear that a comparison is of dubious value. However the nonlinear analyses (*vide infra*) have shown that for relatively large ϵ only small changes from the linear-theory results occur and hence we shall proceed. G & H showed that the effect of the vertical cylindrical wall on the spin-up process was small, and gave several different approximate forms for their results. Note that in the expressions from G & H which follow time is non-dimensionalized by Ω_i^{-1}, and the zonal flow varies from zero initially to unity finally. An expression from their paper [G & H, equation (3.18)] for the interior zonal flow which is valid for short times with respect to the spin-up time but not for a diffusion time is[1]

$$v_I = -2\mathscr{I}\{(2i)^{-\frac{1}{2}}\operatorname{erf}(2it)^{\frac{1}{2}} - (2i - E^{\frac{1}{2}})^{-\frac{1}{2}}\exp(-E^{\frac{1}{2}}t)\operatorname{erf}[(2i - E^{\frac{1}{2}})^{\frac{1}{2}}t^{\frac{1}{2}}]\}. \tag{16}$$

Equation (16) can be rewritten in the following form which is more suitable for numerical evaluation:

$$v_I = 2S(2t) - 2\exp(-E^{\frac{1}{2}}t)\int_0^t \frac{\sin 2\alpha}{(\pi\alpha)^{\frac{1}{2}}}\exp(E^{\frac{1}{2}})\alpha\,d\alpha, \tag{17}$$

where

$$S(2t) = \int_0^t \frac{\sin 2\alpha}{(\pi\alpha)^{\frac{1}{2}}}\,d\alpha.$$

St Maurice & Veronis (1975) have also obtained (17) using a multi-scaling analysis.
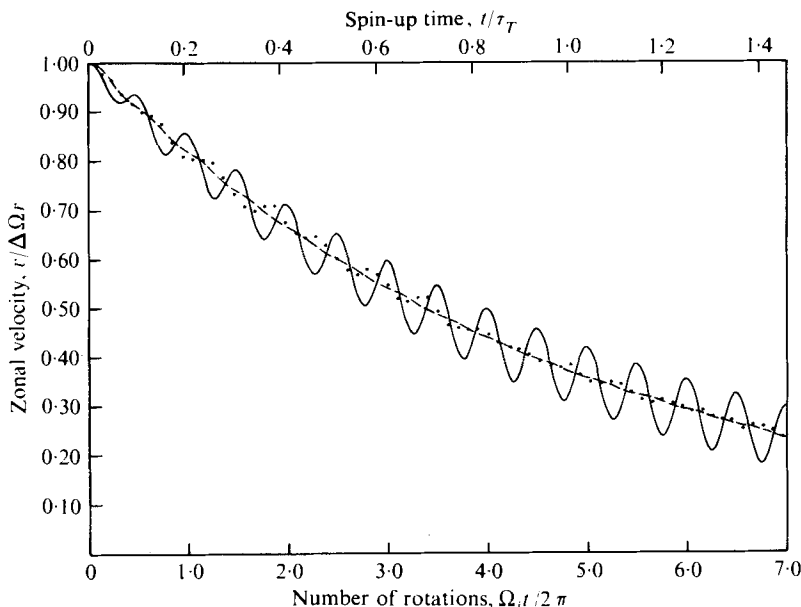
FIGURE 19. Comparison of the experimental results in figure 11 (a) ($E = 1.10 \times 10^{-3}$ and $\epsilon = +0.111$) with the analytical results of Greenspan & Howard (1963). Curves as in figure 18.

Figure number	$E \times 10^3$	ϵ	τ_T	$\bar{\tau}_E$	N	μ
8(a)	3.30	+0.111	2.77	2.78	3	0.05
	3.30	+0.222	2.77	2.75	3	0.04
8(b)	3.30	+0.333	2.77	2.64	3	0.02
9(a)	1.65	+0.111	3.91	3.92	3	0.02
10	1.67	+0.222	3.90	3.81	3	0.01
9(b)	1.58	+0.333	4.00	3.83	3	0.02
11(a)	1.10	+0.111	4.80	4.85	3	0.01
11(b)	1.06	+0.222	4.91	4.78	3	0.01
	2.97	−0.100	2.92	2.86	2	0.02
12	1.49	−0.100	4.13	4.21	2	0.00

TABLE 3. A comparison between the theoretical spin-up time τ_T and the measured average spin-up time $\bar{\tau}_E$ for experiments in which E and ϵ were varied. The location was at the midradius and middepth ($r = 4.75$ cm, $z = 3.00$ cm). Experiments are identified by the figure number in which the results are presented except where additional results have been included.

Figures 18 and 19 show (17) plotted against the small-ϵ results of figures 8 (a) and 11 (a), respectively. G & H also give an approximate form of (17) [G & H, equation (3.20)], namely

$$v_I = 2S(2t)[1 - \exp(-E^{\frac{1}{2}}t)]. \tag{18}$$

Equation (18) is also plotted in figures 18 and 19. Note that for these plots (17) and (18) were transformed to show the decay of a non-dimensional zonal flow of unity to

Figure number	r (cm)	z (cm)	$E \times 10^3$	τ_T	$\bar{\tau}_E$	N	μ
13(a)	2·37	0·75	1·65	3·92	3·85	2	0·04
	2·37	1·50	1·65	3·92	3·83	2	0·00
13(b)	2·37	3·00	1·64	3·93	3·88	2	0·00
14(a)	2·37	4·50	1·64	3·93	3·98	2	0·04
14(b)	2·37	5·25	1·64	3·93	3·86	2	0·01
15(a)	4·75	0·75	1·65	3·92	3·75	2	0·00
	4·75	1·50	1·65	3·92	3·81	2	0·02
15(b)	4·75	3·00	1·65	3·92	3·78	2	0·02
	4·75	4·50	1·65	3·92	3·84	2	0·10
16(a)	7·12	0·75	1·64	3·93	3·58	2	0·00
	7·12	1·50	1·64	3·93	3·55	2	0·04
16(b)	7·12	3·00	1·64	3·93	3·69	2	0·04
	7·12	4·50	1·64	3·93	3·61	2	0·01

TABLE 4. A comparison between the theoretical spin-up time τ_T and the measured average spin-up time $\bar{\tau}_E$ for experiments in which the location alone was varied. The values for E were as shown and the value for ϵ was $+0\cdot222$. Experiments are identified by the figure number in which the results are presented except where additional results have been included.

zero *vs.* time non-dimensionalized by $2\pi\Omega_i^{-1}$. G & H give a third expression [G & H, equation (3.10)] which is valid for spin-up and diffusion times but not for shorter times. This expression is not plotted in this paper since the experimental results are for time periods of about $1\frac{1}{2}$ spin-up times.

The above comparisons show that there is good agreement for the overall decay of the zonal flow (see below) but the inertial oscillations are not described well either in phase or amplitude by the G & H analysis. For the infinite geometry all axisymmetric modes have a frequency of 2Ω, whereas the resonances in the cylinder are given by (15). This frequency difference, as well as the frequency change in the experiments due to the change in Ω, as discussed above, account for the phase errors. The amplitudes given by (17) are too small and those given by (18) are too large. Note also that (17) and (18) do not give the z structure of the modes.

Tables 3 and 4 show a comparison between the spin-up times predicted by (18) $(\tau_T = (2\pi)^{-1}E^{-\frac{1}{2}})$ and the spin-up times for the laboratory experiments (τ_E). The spin-up times for additional experiments not presented in §4 have been included in tables 3 and 4. It was not considered worthwhile to show all these results in §4. The values of τ_E were derived using a least-squares fit to a log-linear plot straight line. Since all of the experiments were repeated more than once, an average value $(\bar{\tau}_E)$ of τ_E is given in the tables and the number of repeated experiments N and the standard deviations μ are also given. Although μ is not a good measure of the repeatability of the experiments, because of the small values of N, it does convey some information and so it has been included. Table 3 shows the comparison for fixed r and z and variable E and ϵ and table 4 that for fixed E and ϵ and variable r and z. The agreement between τ_T and $\bar{\tau}_E$ is very good for small ϵ and small r. However, there is a trend towards smaller values of $\bar{\tau}_E$ as ϵ increases and also a similar trend as r increases.

The linear analysis by G & H has been extended to include nonlinear effects by Greenspan & Weinbaum (1965), Venezian (1969), Benton (1973) and Ingersoll &
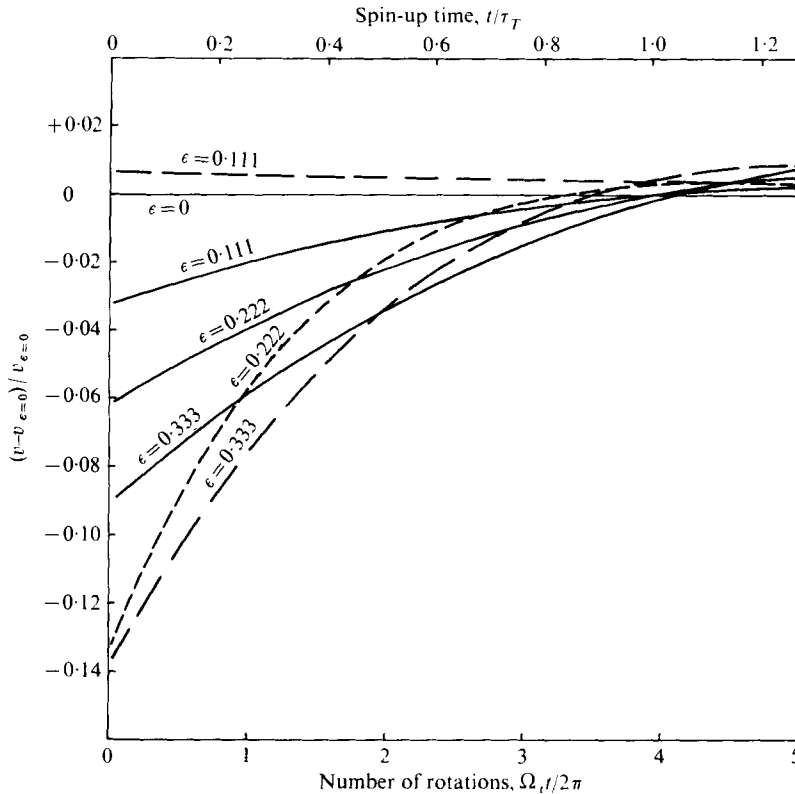
FIGURE 20. Comparison of the experimental results in figures 9(a), 10, 9(b) ($E = 1.65 \times 10^{-3}$, 1.67×10^{-3}, 1.58×10^{-3} and $\epsilon = +0.111$, $+0.222$, $+0.333$, respectively) with the nonlinear results of Greenspan & Weinbaum (1965). The results are plotted for the different values of ϵ as $(v - v_{\epsilon=0})/v_{\epsilon=0}$ vs. the number of rotations, where $v_{\epsilon=0}$ is the zonal flow for $\epsilon = 0$ (the linear case). ——, theory; – – –, experimental results.

Venezian (1968). For all the nonlinear analyses, time is scaled using the spin-up time and hence the inertial modes are excluded. Greenspan & Weinbaum (1965) and Benton (1973) examined the flow between infinite parallel disks for finite ϵ and their results show that for $E^{\frac{1}{2}} \ll 1$ and $0 < \epsilon < 0.3$ only small quantitative changes from the linear theory occur in the flow. Their results show that initially spin-up proceeds less rapidly than the linear theory predicts and then later spin-up proceeds more rapidly. The cross-over point occurs at a time equal to 1.02 times the spin-up time. Figure 20 shows a comparison between the results of Greenspan & Weinbaum (1965) and the experimental results in figures 9 (a), 10 and 9 (b). Because of the smallness of the effects due to nonlinearity, it was necessary in preparing this plot to smooth out the inertial modes present in the experimental results; this was done by fitting the data to a low power law curve. The theory and experiments show the same trend due to nonlinearity and agreement with respect to the cross-over point is good. It is these departures from the exponential decay of the linear theory which account for the decrease of $\bar{\tau}_E$ with increasing ϵ shown in table 3.

Venezian (1969) and Ingersoll & Venezian (1968) examined the spin-up flow in a cylinder for finite ϵ and their results indicate the existence of two interior flow regions

divided by a moving front. The outer flow region is effectively spun-up. The front starts at the outer wall and moves inwards according to

$$r^* = b(1+\epsilon)^{-\frac{1}{2}}[1+\epsilon\exp(-E^{\frac{1}{2}}t)]^{\frac{1}{2}}, \tag{19}$$

where r^* is a dimensional radius and t has been non-dimensionalized by the final rotation rate. Thus for $\epsilon = 0.222$ and $t \to \infty$, $r^* \to 8.58$ cm. Venezian (1969) has also shown that the front has a thickness of $2E^{\frac{1}{4}}h$, which for the results in table 4 ($E = 1.65 \times 10^{-3}$) is equal to 1.22 cm. Since the above thickness is only a characteristic value it is not unreasonable to expect that the outer flow region is making its presence felt at the outermost measurement location of $r = 7.12$ cm and even at $r = 4.75$ cm. This is suggested as the reason for the decrease in $\bar{\tau}_E$ with increasing radius shown in table 4.

In a recent publication Weidman (1976) reports on laser-Doppler measurements of linear and nonlinear spin-up and spin-down for a cylindrical container undergoing a constant angular acceleration. This paper contains many valuable results for very small Ekman numbers ($\sim 10^{-7}$). However, the velocimeter used was stationary in the laboratory frame and could not measure phenomena on the time and space scales of the inertial waves. Weidman also determined the stability boundary for Ekman spiral waves during spin-up and the stability boundary for Couette flow instability for spin-down.

6. Conclusions

The spin-up flow in a cylinder of homogeneous fluid has been examined both experimentally and numerically. The primary motivation for this work was to check numerical solutions by comparing them against accurate and disturbance-free laboratory measurements obtained with a rotating laser-Doppler velocimeter. For the ranges of E and ϵ considered ($1.06 \times 10^{-3} \leqslant E \leqslant 3.30 \times 10^{-3}$, $0.10 \leqslant |\epsilon| \leqslant 0.33$), the spin-up flow is an axisymmetric and dissipative flow with strong rotational effects and weak nonlinear effects.

The numerical work used the primitive equations in axisymmetric form and was conducted on staggered grids for both constant and variable spacing. Different differencing schemes were used for the constant and variable grids. The results show the stretched-grid code to be superior to the constant-grid code. The constant-grid code requires many more points in the mesh and hence excessive computer time for the correct simulation of the boundary-layer dynamics. The increased truncation error due to the grid stretching and the poorer resolution in the interior region do not offset at all the improvement gained by the correct boundary-layer simulation. However, it should be noted that, for this problem, because of the Taylor–Proudman constraint there is not much vertical structure in the interior. Resolution studies established that at least six grid points must be located between the wall and the first maximum of the Ekman-layer radial velocity profile in order for the spin-up times to stabilize to constant values. Using the stretched-grid code the interior resolution was tested by doubling the grid size from 42×42 to 82×82 but the results showed that no changes in the spin-up times occurred for these resolutions as long as the above condition on Ekman-layer resolution was satisfied.

The asymptotic numerical results still have errors arising from the truncations of the finite-differencing schemes. The effect of these errors was assessed by comparing

the numerical simulations with the experimental results. These comparisons yielded differences almost all of which are within the experimental tolerance of a few per cent. Thus the accuracy of the numerical schemes has been established for this type of flow.

The experimental results were compared with the linearized analysis of Greenspan & Howard (1963) and the nonlinear analysis of Greenspan & Weinbaum (1965). Both of these analyses are for infinite parallel disks and only the former includes the inertial oscillations. In spite of the geometrical differences between the theory and the experiments, the theory predicts that the overall decay of the zonal flow on the spin-up time scale should be very similar for both geometries and, in fact, very good agreement was obtained. The weak nonlinear effects are detectable in the experimental results and show the trends predicted by the theory. The inertial modes for two infinite disks are substantially different from those for a cylinder of the dimensions used for the experiments $(2h/b = 0.636)$ and agreement between theory and experiment, as expected, was not good. The experimental results show the correct frequency and z structure for the expected inviscid cylinder mode $(m = 2, n = 1)$; however there is not agreement with the r structure. Perhaps this discrepancy is due to the moving front discussed in § 5. Some weak amplitude modulation, which is suggestive of the presence of another mode, is also present, especially for the results for lower Ekman numbers.

REFERENCES

ADRIAN, R. J. 1972 Statistics of laser Doppler velocimeter signals: frequency measurement. *J. Phys. E. Sci. Instrum.* **5**, 91.

ADRIAN, R. J. & GOLDSTEIN, R. J. 1971 Analysis of a laser Doppler anemometer. *J. Phys. E, Sci. Instrum.* **4**, 505.

BENTON, E. R. 1973 Nonlinear hydrodynamic and hydromagnetic spin-up driven by Ekman–Hartmann boundary layers. *J. Fluid Mech.* **57**, 337.

BENTON, E. R. & CLARK, A. 1974 Spin-up. *Ann. Rev. Fluid Mech.* **6**, 257.

BRYAN, K. 1966 A scheme for numerical integration of the equations of motion on an irregular grid free of non-linear instability. *Mon. Weath. Rev.* **94**, 39.

CERASOLI, C. P. 1975 Free shear layer instability due to probes in a rotating source–sink flow. *J. Fluid Mech.* **72**, 559.

FOWLIS, W. W. & MARTIN, P. J. 1975 A rotating laser Doppler velocimeter and some new results on the spin-up experiment. *Geophys. Fluid Dyn.* **7**, 67.

FULTZ, D. & KAISER, J. A. C. 1971 The disturbing effects of probes in meteorological fluid-model experiments. *J. Atmos. Sci.* **28**, 1153.

GEORGE, W. K. & LUMLEY, J. L. 1973 The laser-Doppler velocimeter and its application to the measurement of turbulence. *J. Fluid Mech.* **60**, 321.

GREENSPAN, H. P. 1969 *The Theory of Rotating Fluids.* Cambridge University Press.

GREENSPAN, H. P. & HOWARD, L. N. 1963 On a time-dependent motion of a rotating fluid. *J. Fluid Mech.* **17**, 385.

GREENSPAN, H. P. & WEINBAUM, S. 1965 On non-linear spin-up of a rotating fluid. *J. Math. Phys.* **44**, 66.

HARLOW, F. H. & WELCH, J. E. 1965 Numerical calculation of time dependent viscous incompressible flow of fluid with free surface. *Phys. Fluids* **8**, 2182.

INGERSOLL, A. P. & VENEZIAN, G. 1968 Non-linear spin-up of a contained fluid. *Div. Geol. Sci., Calif. Inst. Tech. Contr.* no. 1612.

PIACSEK, S. A. & WILLIAMS, G. P. 1970 Conservation properties of convection difference schemes. *J. Comp. Phys.* **6**, 392.

ST-MAURICE, J.-P. & VERONIS, G. 1975 A multi-scaling analysis of the spin-up problem. *J. Fluid Mech.* **68**, 417.

VENEZIAN, G. 1969 Spin-up of a contained fluid. *Topics in Ocean Engng* **1**, 212.

WACHPRESS, E. L. 1966 *Iterative Solution of Elliptic Systems*. Prentice-Hall.

WEIDMAN, P. D. 1976 On the spin-up and spin-down of a rotating fluid. Part 2. Measurements and stability. *J. Fluid Mech.* **77**, 709.

WILLIAMS, G. P. 1969 Numerical integration of the three-dimensional Navier–Stokes equations for incompressible flow. *J. Fluid Mech.* **37**, 727.

YEH, Y. & CUMMINS, H. Z. 1964 Localized fluid flow measurements with a He–Ne laser spectrometer. *Appl. Phys. Lett.* **4**, 176.